PRIFYSGOL BANGOR / BANGOR UNIVERSITY

Water-level controls on macro-tidal rip currents

Austin, M.J.; Masselink, G.; Scott, T.M.; Russell, P.E.

Continental Shelf Research

DOI:
10.1016/j.csr.2013.12.004

Published: 16/12/2013

Publisher's PDF, also known as Version of record

Cyswllt i'r cyhoeddiad / Link to publication

Dyfyniad o'r fersiwn a gyhoeddwyd / Citation for published version (APA):
Austin, M. J., Masselink, G., Scott, T. M., & Russell, P. E. (2013). Water-level controls on macro-tidal rip currents. *Continental Shelf Research*, *75*, 28-40. https://doi.org/10.1016/j.csr.2013.12.004

Hawliau Cyffredinol / General rights
Copyright and moral rights for the publications made accessible in the public portal are retained by the authors and/or other copyright owners and it is a condition of accessing publications that users recognise and abide by the legal requirements associated with these rights.

• Users may download and print one copy of any publication from the public portal for the purpose of private study or research.
• You may not further distribute the material or use it for any profit-making activity or commercial gain
• You may freely distribute the URL identifying the publication in the public portal ?

Take down policy
If you believe that this document breaches copyright please contact us providing details, and we will remove access to the work immediately and investigate your claim.

05. May. 2023

Continental Shelf Research 75 (2014) 28–40

Contents lists available at ScienceDirect

Continental Shelf Research

journal homepage: www.elsevier.com/locate/csr

Research papers

Water-level controls on macro-tidal rip currents

Martin J. Austin [a,*,1], Gerd Masselink [b], Tim M. Scott [b], Paul E. Russell [b]

[a] School of Ocean Sciences, Bangor University, Menai Bridge, Anglesey LL59 5AB, UK
[b] School of Marine Science and Engineering, Plymouth University, Drake Circus, Plymouth PL4 8AA, UK

ARTICLE INFO

Article history:
Received 23 July 2013
Received in revised form
29 November 2013
Accepted 3 December 2013
Available online 17 December 2013

Keywords:
Rip current
Macro-tidal
Water-level
Set-up
Surf zone

ABSTRACT

Field measurements and numerical modelling have been used to investigate the water-level control of rip current dynamics on a macro-tidal beach. Field data collected over 32 complete tidal cycles, spanning a range of wave and tide conditions, demonstrate that rip current strength and behaviour is modulated at the semi-diurnal frequency by tide-induced changes in the water-level over bar/rip morphology. Peak flow speeds in the rip neck $\langle uv \rangle$ correspond to the time of maximum wave breaking 1.5 h before and after low water.

Alongshore-directed water surface gradients $\partial\eta/\partial y$ were measured along the feeder channel and around the ends of the inter-tidal bar, with head differences $O(0.1\ \mathrm{m})$. The numerical model reproduced $\partial\eta/\partial y$ with a good level of skill and showed that $\partial\eta/\partial y$ and $\langle uv \rangle$ increase with the proportion of breaking waves Q_b over the inter-tidal bar; but $\langle uv \rangle$ was maximised during peak Q_b, maximum $\partial\eta/\partial y$ occurred when wave breaking moved offshore to the sub-tidal bar and Q_b was reduced. Around low water, the forcing of the rip current by the alongshore pressure-driven feeder current was reduced by the decrease in Q_b over the bar and feeder regions, but an offshore flow through the rip channel was maintained by a localised intensification of $\partial\eta/\partial y$ around the ends of the inter-tidal bar.

© 2014 The Authors. Published by Elsevier Ltd. Open access under CC BY license.

1. Introduction

Studies of rip currents in energetic macro-tidal environments have been limited (e.g. Bruneau et al., 2009; Austin et al., 2010), but have identified the strong tidal modulation of rip current speed and activity. Macro-tidal rip currents are typically associated with extensive, well-developed 3D morphology located around the spring low-tide limit, where there is sufficient tidal stationarity to allow large length-scale bar/trough systems to develop (Masselink and Short, 1993; Scott et al., 2011). The majority of previous studies have focused on micro-tidal environments where the length-scale of the bed perturbations is relatively small (e.g. McKenzie, 1958; MacMahan et al., 2008).

Large bathymetric non-uniformities lead to large spatial gradients in the depth-induced transformation of short waves across the nearshore. Radiation stresses are forced by this short wave transformation (Bowen, 1969) and during wave breaking energy is also transferred to the roller, which becomes an additional source of radiation stress (Deigaard, 1993). The set-up gradients within the surf zone are balanced by the formation of pressure gradient forces, leading to significant pressure-driven currents (e.g. Haas et al., 2003). Haller et al. (2002) analysed the alongshore momentum balance during a set of laboratory experiments and demonstrated that the magnitude of the alongshore rip feeder current was controlled by the balance between the alongshore pressure gradient force generated by high set-up over the bar crests and the opposing radiation stress gradient generated by larger waves propagating into the rip channel. The region of maximum feeder strength was also shifted into the trough landwards of the inter-tidal bar. These observations complement those of Nielsen et al. (2001), who measured the total water-level over-height landward of the bar driving the alongshore feeder channel.

Rapid changes in the water level in macro-tidal environments also provide a significant temporal control on rip current activity. The control is twofold: (1) changes in water level modulate the expression of the morphology (Castelle et al., 2006; Austin et al., 2010); and (2) result in limited stationarity across the nearshore and hence the rapid cross-shore translation of the surf zone. These two processes combine, to effectively switch the rip currents on and off several hours before and after low water, respectively, by controlling the spatial pattern of wave energy dissipation and thus the formation of the pressure-driven currents.

When bar/rip morphology is well-developed, rip flows become increasingly channelised by the morphology around low water (Brander, 1999; Austin et al., 2010). The emergence of the bar crests, over which waves are breaking, probably reduces the

* Corresponding author. Tel.: +44 1248382803.
E-mail address: m.austin@bangor.ac.uk (M.J. Austin).
[1] Previously at: School of Marine Science and Engineering, Plymouth University, Drake Circus, Plymouth PL4 8AA, UK.

0278-4343 © 2014 The Authors. Published by Elsevier Ltd. Open access under CC BY license.
http://dx.doi.org/10.1016/j.csr.2013.12.004

pressure-driven alongshore feeder current forcing of the rip currents. Significantly, although rip flows were reduced during these periods, they did not stop. One of the key observations of both Brander (1999) and Austin et al. (2010) was that water draining directly from the ends of the emergent inter-tidal bars appeared to be the main forcing for the rip currents at this extremely low stage of the tide; however, this drainage was not quantified.

The limited tidal stationarity of macro-tidal beaches introduces significant challenges to making field measurements. Arrays of sensors deployed across the complex bar/rip morphology dry-out at different times and it becomes difficult to obtain a complete synoptic overview of the rip circulation and forcing when water depths are very shallow. When combined with field observations, numerical modelling becomes a powerful tool to obtain additional information across the very shallow inter-tidal beachface. Several recent studies have used depth-averaged modelling approaches based on field measurements to investigate rip current hydrodynamics (e.g. Castelle et al., 2006; Bruneau et al., 2011). These studies have demonstrated that these models can reproduce wave-driven rip current circulation forced by wave groups (Reniers et al., 2006; Austin et al., 2013) or shear instabilities (Haller and Dalrymple, 2001).

The purpose of this paper is to investigate the dynamics of rip current flows on a macro-tidal beach around the period of dominant rip activity at low water. We hypothesise that the rip currents are forced by a combination of the wave dissipation-induced radiation stress gradient and locally generated water surface gradients around the terminal ends of the inter-tidal sandbars. We use Eulerian and Lagrangian field observations collected around well-developed low tide bar/rip morphology during a period of large spring tides and moderate wave conditions to quantify the rip current flow and forcing. The field data is augmented by a 2D depth-averaged wave/flow model, which is used to quantify the nearshore distribution of short-wave dissipation and the presence of alongshore water surface gradients.

2. Methodology

2.1. Study site

During October 2011 a 16-day field experiment was conducted at Perranporth beach, Cornwall, UK over a spring–neap–spring tidal cycle (Fig. 1). Perranporth is a macro-tidal beach with a semi-diurnal tidal regime and a mean spring range of 6.3 m. It is classified as a low tide bar/rip beach (Scott et al., 2011) and thus exhibits a pronounced inter-tidal bar/rip morphology around the Mean Low Water Spring (MLWS) region and a sub-tidal bar, which vary on seasonal and storm-event timescale. The intertidal beach is relatively flat ($\tan\beta = 0.015$–0.025) and the beach is composed of medium quartz sand ($D_{50} = 0.34$ mm). The beach faces west–northwest and is predominantly exposed to Atlantic swell, but also receives locally generated wind waves (typically from the north). A directional wave rider (DWR) buoy is located close inshore in approximately 13 m water depth, and reported an annual average significant wave height and a peak period of $H_s = 1.4$ m and $T_p = 10.5$ s, respectively, between 2006 and 2012.

2.2. Field experiment

In situ instrument rig arrays were deployed around the MLWS shoreline region to record water level, wave height and flow velocity across the inter-tidal bar, feeder and rip channels (Fig. 1). Two instrument arrays were deployed. The first was an array of three rigs over the intertidal bar (R1, R2 and R4), each mounting a pair of bi-directional miniature electromagnetic current meters (EMCM) and a high-precision pressure transducer (PT). The second array was orientated across the feeder and rip channel with two rigs along the feeder channel (R5 and R6), each mounting a 3D-Acoustic Doppler Velocimeter (ADV) and a PT, and two rigs (R7 and R8) in the rip channel, each also mounting a 3D-ADV and a PT. Four additional bottom-mounted self-recording PT's were deployed around the bar/rip region and a further two were deployed $\sim$500 m offshore to record the wave conditions input to the beachface. The beachface PT's were buried $\sim$0.25 m to measure hydrostatic pressure and avoid contamination of the water-level signal by the dynamic pressure variation (i.e. accelerating/decelerating flows reducing/enhancing pressure). All of the instrument rigs were self-recording and sampled at 4 Hz. This instrument configuration was designed to maximise the spatial coverage over the bar/rip system and data were sampled over a total of 33 complete tidal cycles.

Fifteen GPS-tracked surf-zone drifters were used to record the Lagrangian currents over the bar/rip system. The drifters were of a robust design modified from that of Schmit et al. (2003), Spydell et al. (2007), and MacMahan et al. (2009), and were modular in

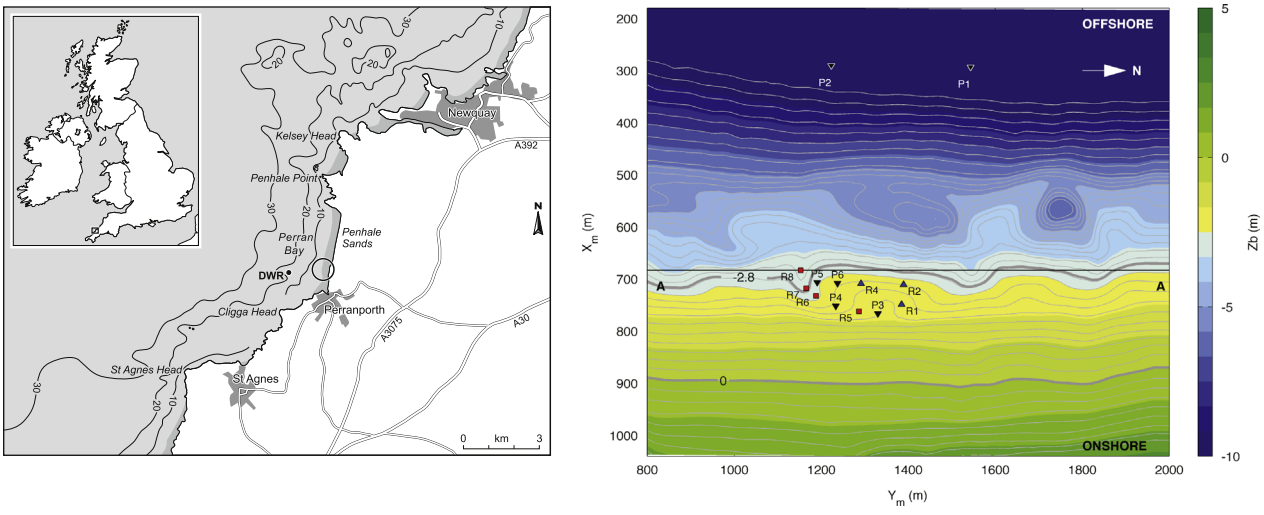

Fig. 1. (Left) Location map of Perranporth indicating the experimental region (circled) and the nearshore directional wave-rider buoy (DWR). (Right) Perranporth bathymetry and instrument locations transformed onto the XBeach model grid. Shading indicates bottom elevation relative to Ordnance Datum Newlyn (ODN) and is contoured at 0.5 m intervals. Heavy contours plot the MLWS and MSL elevations. Alongshore transect A–A is indicated.

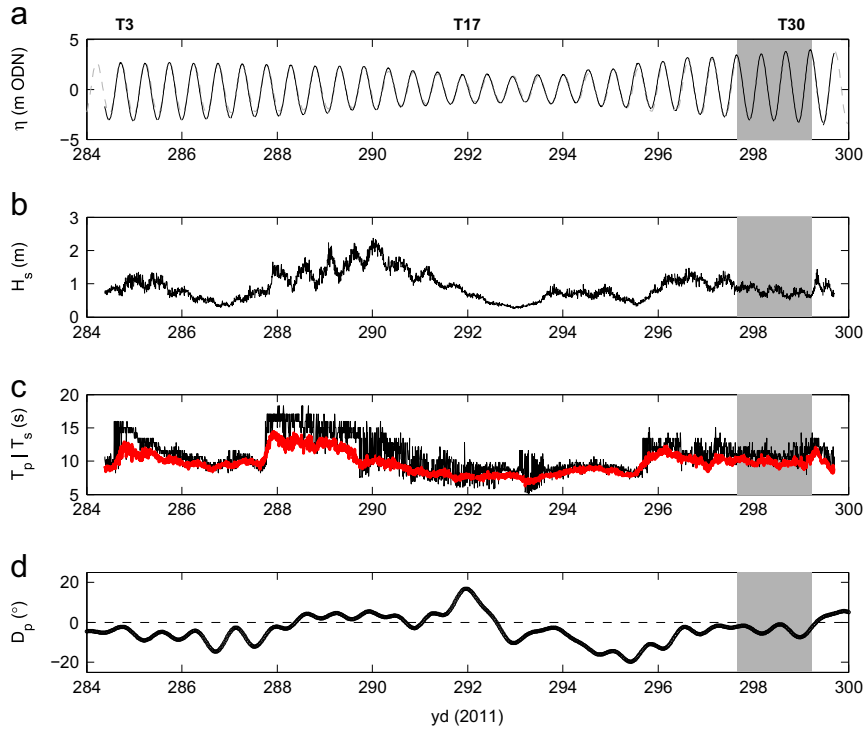

Fig. 2. Nearshore wave and tide forcing during the field experiment. (a) Tidal elevation η; (b) significant wave height H_s; (c) peak T_p (black) and significant T_s (red) wave period; and (d) peak wave direction D_p relative to the shoreline from the nearshore wave buoy versus time. The grey shaded region indicates the period discussed in the following sections. (For interpretation of the references to colour in this figure caption, the reader is referred to the web version of this paper.)

nature allowing any damaged components to be easily replaced in the field. The GPS units were custom-made in-house and recorded the raw L1 GPS carrier-phase information, which was logged to a memory card at 1 Hz. The raw GPS data were post-processed from a static base station to provide an accuracy of <0.4 m in horizontal position and <0.01 m s^{-1} in velocity.

Drifter deployments were for 3–5 h periods centred on low tide when the rip currents were most active. Drifters were individually seeded (rather than in clusters) from the beach into the feeder and rip regions to maintain both spatial and temporal coverage across the bar/rip, maximising the synoptic understanding of circulation patterns through the rip system. Due to the rate of change of tidal elevation within a macro-tidal regime it is desirable to have drifter observations throughout the entire rip system at least for every 30 min. For further details of the drifter data processing, refer to Austin et al. (2013).

The inter- and sub-tidal beach were surveyed regularly throughout the field experiment. Inter-tidal topography (dune foot to MLWS shoreline) was surveyed using a Trimble real-time kinematic (RTK) GPS system mounted on an all-terrain vehicle (ATV) during low tide periods. Sub-tidal bathymetry was collected using RTK-GPS and a single-beam echo sounder mounted onto a personal water craft (PWC) during high tide. Bathymetric data were collected along regularly spaced cross-shore transects ($\Delta y = 25$ m), which overlapped with the intertidal survey by approximately 100 m. The ATV and PWC survey datasets were subsequently merged together and interpolated onto a regular grid using a quadratic loess scale-controlled interpolation method (Plant et al., 2002). The in situ instruments were surveyed using a laser total station, with an accuracy of <1 cm.

2.3. Modelling approach

The XBeach model (cf. Roelvink et al., 2009) was used to solve coupled 2D horizontal equations for wave propagation and flow, for varying spectral wave and flow boundary conditions. XBeach includes a non-stationary wave driver with directional spreading, which accounts for wave-group generated surf motions that are important for rip current dynamics (e.g. MacMahan et al., 2004). Wave–current interaction was included in the model using the formulation of Yu and Slinn (2003), where the offshore-directed rip currents impart negative feedback on the wave forcing. For this application, XBeach was run only in hydrodynamic mode without sediment transport or morphological updating to minimise computational time.

The model bathymetry was based on the combined bathymetric and topographic survey data measured during the field experiment at the time nearest to the simulation time of interest. A rectilinear computational grid was generated, which optimised the spatial resolution across the surf zone in the centre of the model domain ($\Delta x = 2$ m, $\Delta y = 5$ m), which is 860 m $\times$ 1220 m in the cross- and alongshore directions, respectively. The wave conditions at the offshore boundary of the XBeach model were described by the 2D spectral output from a nested SWAN model (cf. Austin et al., 2013), appropriate to the simulation time. The tidal level along the offshore boundary of the model was varied over each simulation, based on a local prediction derived from the harmonic analysis of a long-term dataset.

The XBeach model has a number of free parameters that are used to calibrate the model. In this hydrodynamic-only model, the parameters that required tuning were those governing the short-wave breaking: the breaker parameter (γ) and the breaker slope coefficient in the roller model ($\beta = 0.05$). All other parameters were set to their recommended default values. The hydrodynamics of the model were calibrated with measured Eulerian data and the computed nearshore circulation patterns were validated against Lagrangian drifter measurements by Austin et al. (2013).

The advective-deterministic approach (ADA) for wave breaking (Daly et al., 2012) was used ($break=4$). Wave breaking within the ADA model is turned on and off through upper and lower values of

the breaker parameter γ and the state of breaking is advected landwards at the individual wave celerity. Breaking occurs when $H_E > \gamma_b$ and stops when $H_E < \gamma_r$, where H_E is the (energy-based) short wave height, γ_b and γ_r are the breaker and reformation parameters, respectively, and are expressed as follows:

$$\gamma_b = \frac{H_{E,b}}{h} \quad \text{and} \quad \gamma_r = \frac{H_{E,r}}{h} \tag{1}$$

where h is the local water depth. The values of the breaker parameters used were $\gamma_b = 0.55$ and $\gamma_r = 0.3$, as calibrated for Perranporth by Austin et al. (2013). For values of H_E between the breaking limits the state of breaking B, which has binary values, propagates with the celerity of the individual wave c_x controlled by the differential in Eq. (3):

$$B = 1, \quad H_E > \gamma_b h \tag{2}$$

$$\frac{\partial B}{\partial t} = c_x \frac{\partial B}{\partial t} = 0, \quad \gamma_r h < H_E < \gamma_b h \tag{3}$$

$$B = 0, \quad H_E < \gamma_r h. \tag{4}$$

Advecting B landward ensures that the wave breaking history is maintained for its duration (while $B=1$) and ensures that premature wave breaking does not occur (Daly et al., 2012). The time-averaged proportion of breaking waves Q_b at any location is therefore the time-average of B at that point, so

$$Q_b = \langle B \rangle. \tag{5}$$

Three model simulations were carried out centred on the low tide periods during yeardays 297–299 (T28–T30). Data were output across the model domain at 30-s intervals and as 10-min averages, while point data were output at 1 Hz at locations corresponding to the instrument rig locations.

3. Results

3.1. Tide and wave conditions

Water levels and nearshore waves were measured using PT2 located 500 m seaward of the low tide surf zone in 12 m water depth and directional wave rider buoy located 1 km offshore in 15 m of water (Fig. 2). Tidal range varied between 2.5 m and 7.3 m and progressed from springs to neaps and returned to springs during the experiment (yearday 284–300). Wave height and peak period varied between 0.4 m and 2.4 m and between 6 s and 18 s, respectively. Wave direction was relatively shore-normal, but reflects the influence of westerly swell waves and northerly wind seas, with the exception of yearday 295 when strong southerly winds were experienced. Herein we analyse the data collected during yeardays 297–299 (T28–30) when the forcing conditions remained relatively constant with moderate-energy, approximately shore-normal, waves ($H_s = 0.9$ m; $T_p = 12$ s) and large spring tide ranges; we therefore assume that changes in the rip dynamics are primarily due to tidal variations.

3.2. Mean rip characteristics

The mean Lagrangian currents measured using GPS drifters during T30 indicate a complex circulation pattern across the low tide surf zone (Fig. 3). Drifter data were averaged into 10×10 m spatial bins across two temporal windows, one reflecting the mid-tide period -2.5 to -0.5 h $<$ LT $<$ 0.5–2.5 h when the rip was generally active, and the other at low tide -0.5 h $<$ LT $<$ 0.5 h when the rip is more constrained. Only bins with greater than 3 degrees of freedom were included in the averaging.

At mid-tide, currents flow offshore through the rip channel at [$X_m = 720$ m, $Y_m = 1200$ m] before turning alongshore and flowing principally northwards in the trough between the inter- and sub-tidal bars; some flow splits-off to the south. The current then

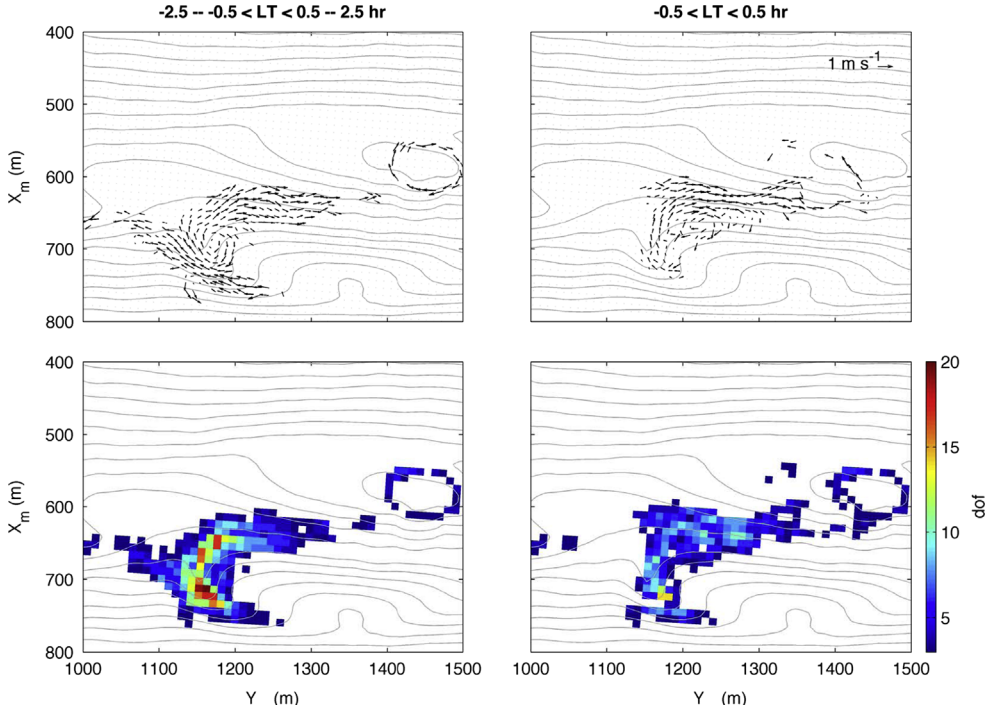

Fig. 3. (Top) The mean rip circulation pattern averaged within 10×10 m bins over the periods -2.5 to $-0.5 <$ LT < 0.5–2.5 h (left) and $-0.5 <$ LT < 0.5 h (right) during T30. Vectors plot rip speed with the scale shown in the top right corner, contours plot bathymetry at 0.25 m intervals. (Bottom) Number of degrees of freedom *dof* within each averaging bin. Bins with *dof* < 3 were discounted.

rotates seawards and circulates across a deep depression in the sub-tidal bar at [$X_m = 600$ m, $Y_m = 1350$ m], reflecting a coupling between the inter- and sub-tidal bar systems.

Around the lowest tidal levels, the overall circulation is similar, but the following key differences are observed: (1) the forcing from the southerly flowing feeder is reduced; (2) the segment of flow splitting-off to the south stops; and (3) the main rip flow is more shore-normal extending ~ 50 m further seaward.

3.3. Kinematic rip characteristics

Time series of Eulerian data collected over T29–T30 at three distinct morphological locations demonstrate the temporal and spatial variability of the surf zone motion (Fig. 4). The semi-diurnal water depth variation is >6.5 m, which modulates the wave height as the surf zone migrates cross-shore. Cross-shore and alongshore flow velocities are typically strongest when $h < 4$ m, and display the greatest variance over the bar crest (R4). Low-frequency motions are also evident in the flow velocity signals, with peaks in the alongshore current (in opposing directions) around low water at R4 and R5, and a corresponding offshore-directed signal at R8.

The water-level spectrum at the bar crest (R4) indicates that the incoming wave field contains significant energy at 12 s and 43 s, corresponding to incident and infragravity waves, respectively. The incident wave peak is also present in the u and v spectra, but the infragravity peak becomes indistinct due to a general increase in low frequency energy. The distribution of energy across the feeder channel (R5) is similar to R4, but the incident wave peak is significantly reduced for h, u and v, due to breaking-induced dissipation across the bar. Within the rip

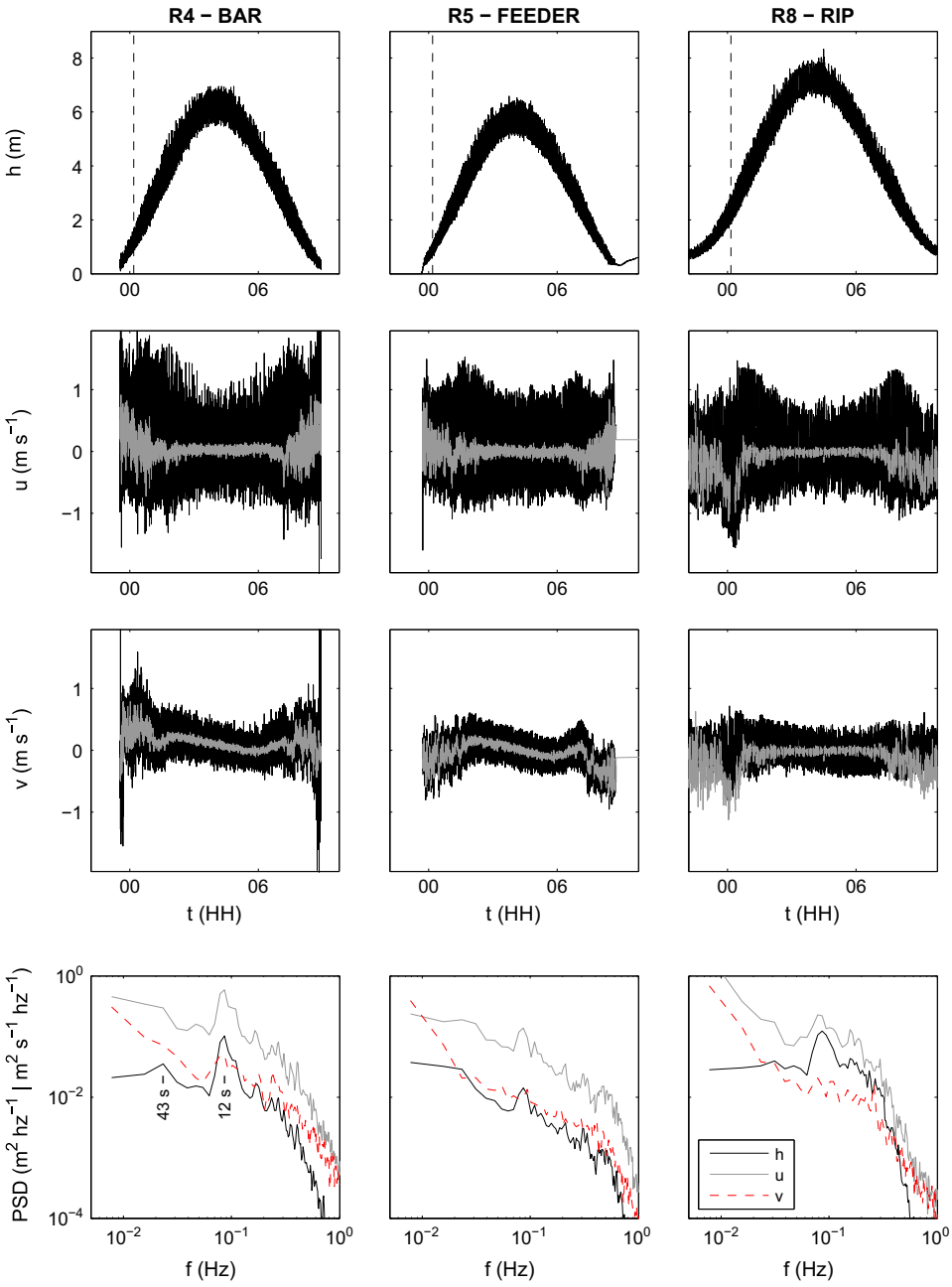

Fig. 4. Example Eulerian time series data collected between low tide T29 and T30. From top: Water depth h; cross-shore flow velocity u (black) and lowpass filtered u (grey; filter cutoff 33 s); alongshore flow velocity v (black) and lowpass filtered v (grey) and (bottom) spectral density for h, u and v indicating the principle incident and infragravity peaks at 12 s and 43 s, respectively. Spectra were computed using Welch's segment-averaging method from 17-min time series with 4096 samples and sixteen 50% overlapping segments. The mean water depth at R4 was 1.2 m (indicated by vertical black dashed line in the upper panels).

channel (R8), the spectrum of h is again similar to R4, but there is no distinct infragravity peak. Instead, there is a general increase in low frequency energy for both u and v.

A number of 10-min mean hydrodynamic parameters were computed from the time series of h, u and v recorded across all of the instrument rigs. The 10-min time series segments were de-trended using a 2nd-order polynomial filter to remove the non-stationary effects of the tidal variation in water-level. The mean cross-shore $\langle u \rangle$ and alongshore $\langle v \rangle$ flow velocities, where $\langle \cdot \rangle$ indicates time-averaging over the 10-min period were computed. Band-passed velocity amplitudes for the cross-shore velocity (U_m) and the alongshore velocity (V_m) were computed as $2\sqrt{\sigma}$, within the infragravity, *ig* (<0.05 Hz) and incident, *ss* (0.05–0.33 Hz) frequency bands, where σ is the variance of the u or v time series. The scalar quantity of the rip speed $\langle uv \rangle$ ($=\langle\sqrt{u^2+v^2}\rangle$) and the relative wave height H/h were also computed.

An ensemble-average of the hydrodynamic conditions within the rip channel (R8) over the three tidal cycles was generated by averaging a number of the parameters defined above relative to the time of low water (T). Fig. 5 indicates that the ensemble is representative of the conditions over an individual tide. Maximum $\langle u \rangle$ occurs 2 h either side of low water and is directed offshore at -0.4 m s^{-1}. Alongshore-directed flows $\langle v \rangle$ are weaker and directed towards the south at (-0.2 m s^{-1}) and peak before $\langle u \rangle$. It is also noteworthy that $\langle v \rangle$ is influenced by the mean tidal currents, flowing north from the mid-flood tide, before reversing to the south at high tide. The cross-shore infragravity velocity amplitude $U_{m,ig}$ begins to increase 4 h before low water, peaking at low water. The relative wave height H/h indicates that wave breaking in the rip channel ($H/h > 0.4$) only occurs in the period 2–3 h either side of low water. At lower tidal levels, depth-induced breaking over the sub-tidal bar reduces H/h in the inner-surf zone.

The hydrodynamic process signature (Wright and Short, 1984) over the bar/rip system was computed to demonstrate the spatial distribution of the important hydrodynamic processes around low water (Fig. 6). Across the inter-tidal bar (R2 and R4), the incident-band signal dominates and is approximately double the magnitude

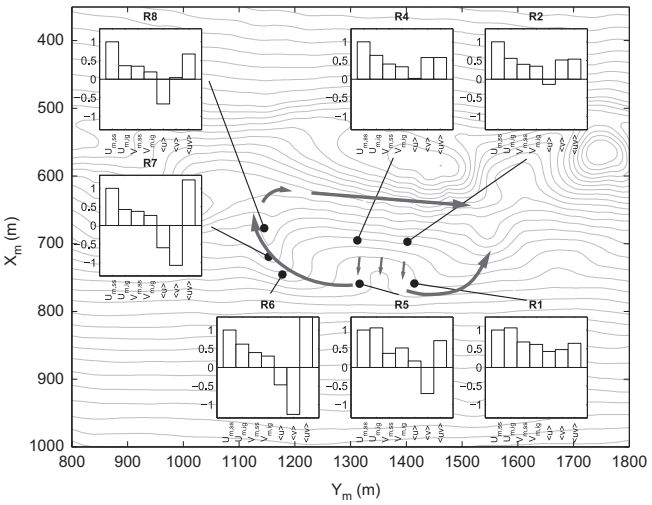

Fig. 6. Snap-shot of the hydrodynamic process signature plotted over the bar/rip morphology for $h=1$ m at R4. Bandpass-filtered velocity amplitude defined as $2\sqrt{\sigma_u}$ (where σ_u is the variance of the velocity time series) for the cross-shore incident $U_{m,ss}$ and infragravity bands $U_{m,ig}$, the alongshore-directed $V_{m,ss}$ and $V_{m,ig}$; the mean time-averaged cross-shore and alongshore-directed currents u, v and the resultant rip speed $\langle uv \rangle$. All quantities are normalised by $U_{m,ss}$ and the sub-plots are arranged to reflect their real-world relative positions. Negative values of $\langle u \rangle$ and $\langle v \rangle$ reflect offshore- and southerly-directed flows, respectively.

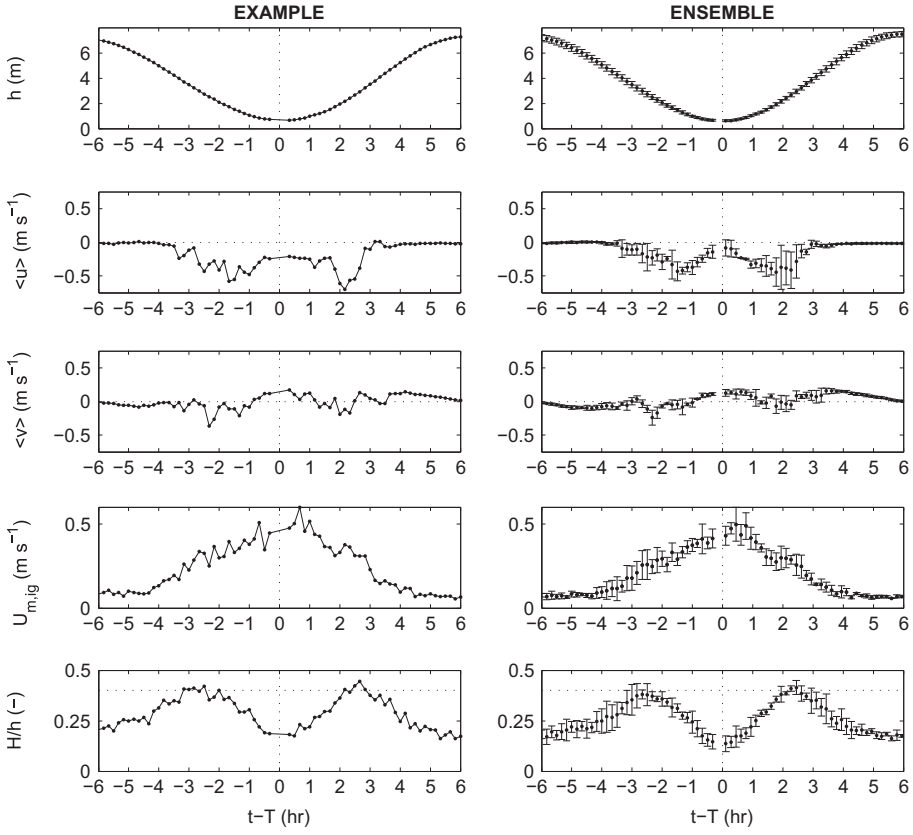

Fig. 5. (Left) Example hydrodynamics collected in the rip channel at R8 during T28 and (right) ensemble-averaged hydrodynamics for T28–T30 versus time relative to high tide (T). From top: 10-min time-averaged water depth h; cross-shore flow velocity $\langle u \rangle$; alongshore flow velocity $\langle v \rangle$; cross-shore infragravity velocity amplitude $U_{m,ig}$; and relative wave height H/h. Error bars are ± 1 standard deviation for the ensemble-average.

of the infragravity-band. At R4 the alongshore-directed mean flow component is important. Landwards of the bar (R1, R5 and R6) the alongshore mean flow component becomes increasingly important moving towards the rip channel, becoming the same magnitude as $U_{m,ss}$ by R6. At the landward end of the rip channel (R7) the alongshore mean flow component dominates, but the cross-shore mean component and both infragravity components are important. At the rip neck (R8), the alongshore component is negligible and the cross-shore mean component is secondary only to $U_{m,ss}$.

This spatial distribution of hydrodynamic processes is indicative of the rip circulation measured by the drifters (Fig. 3). Incoming waves break over the inter-tidal bar, establishing an alongshore current over and seaward of the crest. Landwards of the bar crest, the flow becomes increasingly alongshore dominated towards the rip channel. Due to the morphological configuration, the rip channel cuts across the surf zone at an angle before becoming shore-normal. This is reflected in the flows observed at R7, which were strongly oblique (large $\langle u \rangle$ and $\langle v \rangle$ components) before becoming offshore-directed at R8. The $\langle v \rangle$ component of the flow at R7 probably over-shoots the position of R8, resulting in the negligible alongshore flow at R8.

While the spatial distribution of the hydrodynamic processes is quantified in Fig. 6, there is no temporal information. The ensemble average (Fig. 5) provides confidence that the hydrodynamic process signature can also be averaged over the same three tides. Therefore a temporally averaged process signature for the bar (R4), feeder (R5) and rip channel (R8) locations was computed from the ensemble-averaged hydrodynamics recorded over T28–T30 (Fig. 7).

The bar crest and feeder channel locations dry-out at low water and several clear trends are evident in the data: (1) the relative proportion of $U_{m,ss}$ at all locations increases towards low water, peaking at $t-T=-3$ h, before decreasing and reaching a minima at low water; (2) the proportion of infragravity motions $U_{m,ig}$ increases steadily from <0.2 at high tide and peaks at approximately $t-T=-1.5$ h in the feeder channel; (3) strong alongshore-directed flows are recorded in the feeder channel in the periods either side of low water from $t-T=-3$ to -1 and 1–3 h; (4) strong offshore-directed flows in the rip channel correspond to strong alongshore-directed flows in the feeder during the same period; and (5) the rip continues to flow over low water, despite the lack of forcing from the feeder channel, suggesting an additional forcing process.

The numerical hydrodynamic process signature was also computed to validate the model performance against the field observations.

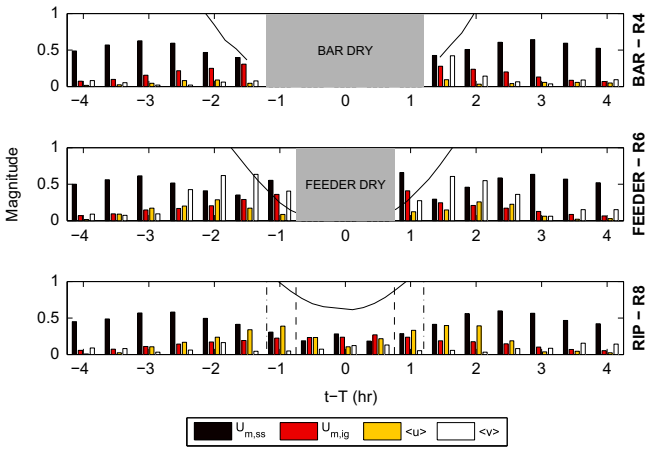

Fig. 7. Temporal evolution of the ensemble-averaged hydrodynamic process signature for T28–T30 at the bar, feeder and rip locations plotted versus time (t) minus time at low tide (T). The black line plots water depth h. Vertical dotted-dash and dashed lines plot times when the bar and feeder, respectively, are dry.

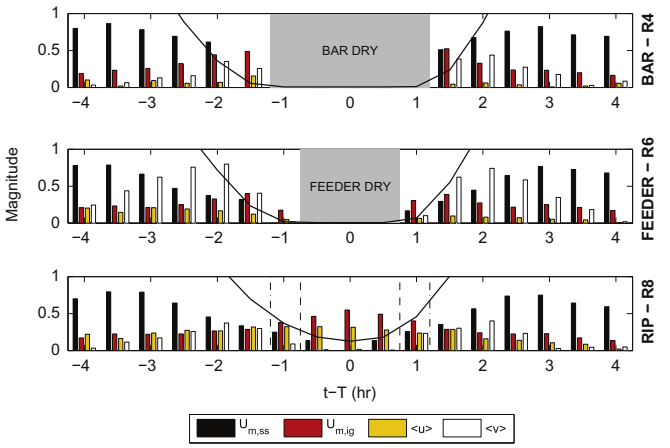

Fig. 8. Modelled temporal evolution of the hydrodynamic process signature at the bar, feeder and rip locations for T30. Black line plots water depth h. Vertical dotted-dash and dashed lines plot times when the bar and feeder, respectively, are dry.

Fig. 8 is the XBeach model equivalent of Fig. 7, and generally reproduces the measured data well, particularly the evolution of the short- and long-wave velocity amplitudes $U_{m,ss}$ and $U_{m,ig}$, and the alongshore flows in the feeder and rip channels. One anomaly is the increase in $U_{m,ss}$ measured within the feeder channel at $t-T=-1$ and 1 h, but not reproduced by the model. This is probably related to the very shallow water depths measured just before the sensor dried-out, but when waves were still propagating into the channel and running-off the end of the bar. The magnitude of the decrease in cross-shore Eulerian flow in the rip channel at low water is under-predicted.

The measured and modelled hydrodynamic process signatures indicate that rip current flow is significantly modulated by the changing tidal level and that the spatial distribution of the different components of the total flow field is temporally variable. In this macro-tidal environment the rip current modulation is such that at high water levels the rip is inactive, only being activated in the period spanning 3 h either side of low water. The numerical model is therefore used in conjunction with the field data to further explore the physical processes occurring around the time of rip activation.

4. Dynamic rip control

4.1. Alongshore water surface gradients

The formation of alongshore-directed water surface gradients ($\partial\eta/\partial y$) during T28–T30 is investigated using the field and numerical data (Fig. 9). Water surface elevation data from the array of individual pressure transducers (P3, P4, P5 and P6, Fig. 1) were used to compute water surface gradients around the bar/rip system. The data from the sensors were dry-out filtered and temporally averaged into 10-min segments and converted to a water surface elevation (η) by reducing the data to ODN using the surveyed vertical instrument elevations. Small remaining elevation offsets were removed by equalising the data by making the (reasonable) assumption that at high tide, when the sensors are significantly seaward of the shoaling wave zone, there is zero mean water surface slope. Using the surveyed horizontal positions of the sensors, $\partial\eta/\partial y$ was computed in the direction of the rip flow between pairs of PTs (i.e. PT3 to PT4 and PT6 to PT5). The corresponding gradients were output from the model at the same spatial locations; data from the three tides were subsequently ensemble-averaged as previously described.

First, the measured and modelled water depths h were compared for PT3 and PT5, with the measured water depths being well reproduced by the model. The water surface elevation difference ($\partial\eta$, not shown) between the horizontally separated PT's is 2–5 cm around 2 h before low water, increasing to 7–15 cm in the shallowest depths. The measured alongshore water surface gradients ($\partial\eta/\partial y$) are generally well reproduced by the model, particularly with respect to their trends, although the amplitudes around low water are slightly over-predicted by the model. There are two key points worth noting. First, during low tidal levels, when wave breaking is transitioning between inter- and sub-tidal bars, the predicted $\partial\eta/\partial y$ increases at a slightly faster rate than the measured values; the curves re-converge around low water. This is probably due to the model not exactly reproducing the spatial and temporal transition of wave dissipation between the inter- and sub-tidal bars. Secondly, in the measured data, $\partial\eta/\partial y$ for PT6–PT5 reverses for $\sim 60-$min at the beginning of the flood tide, which the model does not reproduce.

The measured and modelled water surface gradients are compared to the flow speed $\langle uv\rangle$ at three locations on the beach-face (R5, R7 and R8; Fig. 10). The flow speed, rather than the $\langle u\rangle$ and $\langle v\rangle$ velocity components, is used to minimise any errors introduced by the model not exactly reproducing the rip flow circulation pattern. There is a linear increase in the flow speed for gradients $\partial\eta/\partial y \leq 0.5\times10^{-3}$, above which the speeds remain roughly constant (R8 and R5) or progressively decrease (R7).

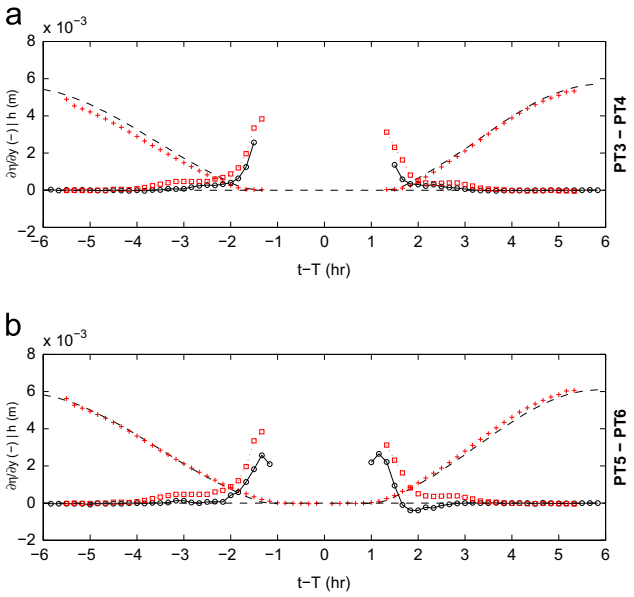

Fig. 9. Ensemble-averaged measured and modelled water surface gradient and depth between PT pairs. (a) Measured (- -) and modelled (+) water depth h ($/10^3$), and measured (○) and modelled (□) alongshore water surface gradient $\partial\eta/\partial y$ for PT3–PT4 in the feeder channel. (b) Same as (a) for PT6–PT5 located at the southern end of the inter-tidal bar.

4.2. Spatial evolution of alongshore gradients

Fig. 11 details the spatial evolution of the modelled alongshore-directed water surface gradient at two intervals during the falling tide of a tidal half-cycle and shows the pattern of wave breaking and the resultant flow field. At $t-T=-2$, spatially variable wave breaking occurs over the bar/rip system and the proportion of breaking waves is clearly reduced over the rip feeder channels. The strong dissipation over the inter-tidal bar crest forces strong flows along the feeder channels, which are reflected in the flow field by wide oblique currents. These diverge from the landward trough of the inter-tidal bar and flow alongshore from the southerly feeder, and offshore to the crescentic sub-tidal bar from the northern feeder.

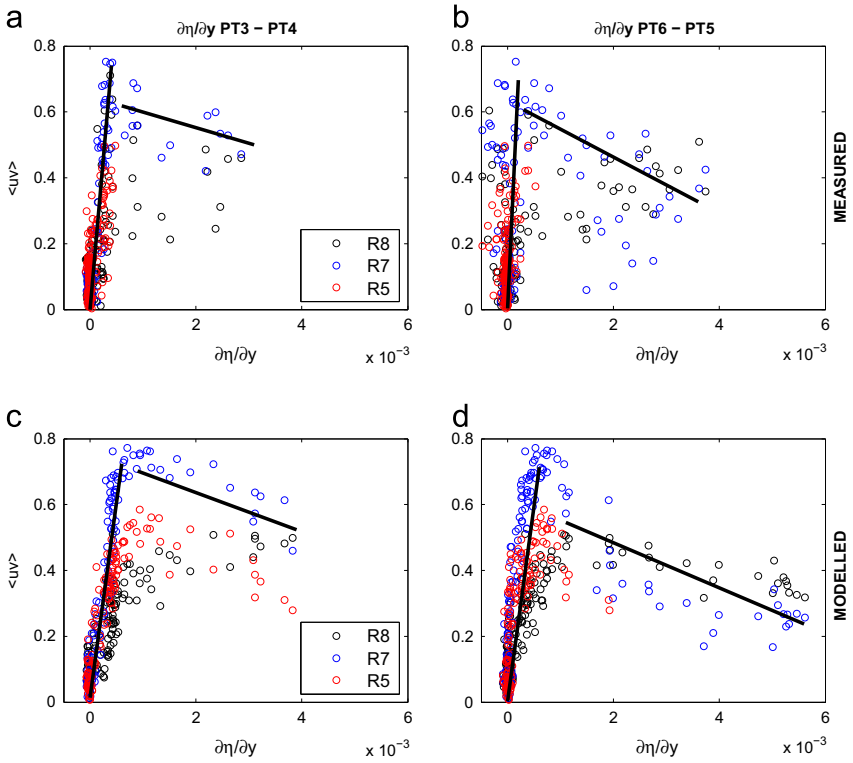

Fig. 10. Temporally averaged flow speed at R5, R7 and R8 as a function of $\partial\eta/\partial y$ in the feeder channel (left) and at the bar end (right). (Top) Measured data along the feeder channel (a) and at the end of the inter-tidal bar (b); (bottom) modelled data from the feeder (c) and bar (d). Solid black lines are a guide to interpretation.

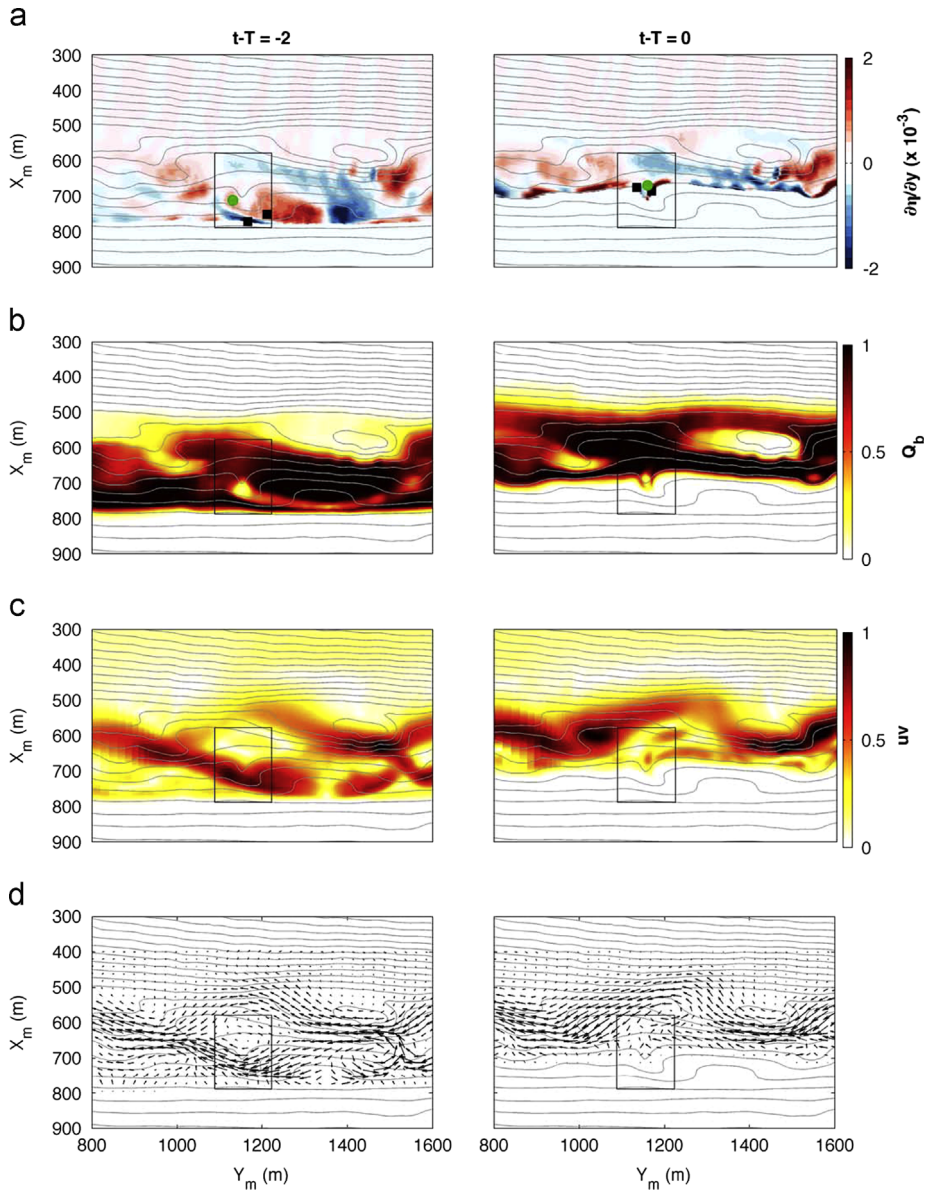

Fig. 11. (a) Modelled 10-min mean alongshore-directed water surface gradient $\partial\eta/\partial y$ at two output times: $t-T=-2$; and at low water $t-T=0$. Hot colours indicate a slope towards the south (left) and cold towards the north (right). Over the region of the rip channel, indicated by the black box, the maxima and minima of the water surface slope are indicated by the black squares and the maximum offshore-directed flow velocity by the green dot; (b) Qb, where darker shading indicates a greater proportion of breaking waves; (c) modelled current speed $\langle uv\rangle$, where darker colours indicate faster speeds; and (d) quiver plot of rip circulation for each output time. (For interpretation of the references to colour in this figure caption, the reader is referred to the web version of this paper.)

Around low water ($t-T=0$), waves break across the sub-tidal bar and the seaward slope of the inter-tidal bar and leave isolated regions with no wave breaking in the centre of the surf zone. Maximum alongshore-directed water surface gradients of the opposite sign exist at the ends of the inter-tidal bar and the maximum offshore-directed rip current velocity is located between and slightly seaward of these maxima. Current velocities over the whole surf zone region are reduced, but the rip current is now a narrow jet, flowing offshore normal to the shoreline, before rotating to the north and feeding the larger-scale circulation over the sub-tidal bar that is exiting the surf zone, as observed in Fig. 3.

4.3. Alongshore non-uniformity

The alongshore non-uniformity of Q_b around the low tide period appears to force the rip current via the highly localised $\partial\eta/\partial y$ around the ends of the bars when the feeder channels are dry and there is no mass flux over the inter-tidal bar. Fig. 12a plots the temporal evolution of $\partial\eta/\partial y$ along transect A–A, which passes through the R8 position (see Fig. 1). Before wave breaking occurs across the nearshore ($t-T=-5$ h), $\partial\eta/\partial y$ is negligible and rip current speeds are low. Mean offshore-directed flows (Fig. 12b) begin to increase at $t-T=-3$ h, when Q_b begins to increase over the inter-tidal bars and as set-up gradients are being established. At $t-T=-2$ h, Q_b starts decreasing over the rip channels and wave breaking primarily occurs over the bar crests (and moves offshore to the sub-tidal bar). Rip flow velocity increases, but the flow is widely distributed over a 200 m wide alongshore region.

Between $t-T=-2$ and $t-T=-1$, a positive (southward acting) $\partial\eta/\partial y$ is established on the northern side of the rip channel ($Y_m=1200$ m). This corresponds to the time when $\langle u\rangle$ increases significantly, the rip speed $\langle uv\rangle$ is maximised and the current becomes increasingly channelised. This positive $\partial\eta/\partial y$ therefore

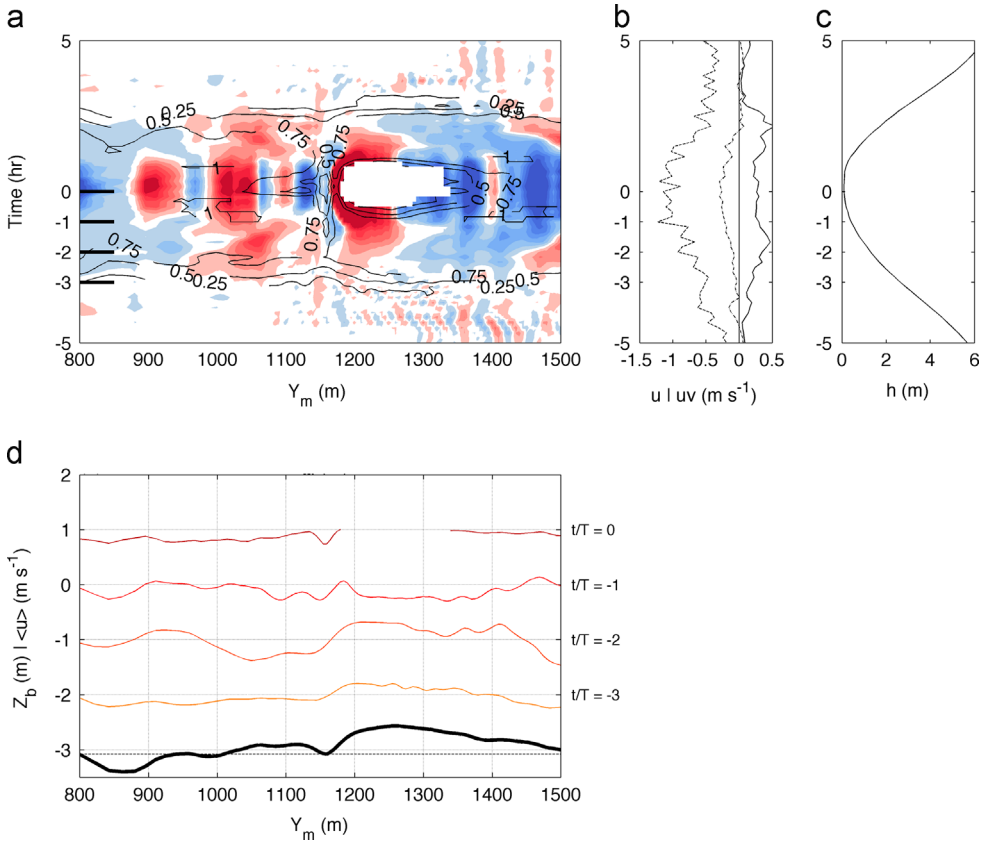

Fig. 12. Water surface gradient. (a) Temporal evolution of the alongshore-directed water surface gradient (shading) along transect A–A. Hot colours indicate a slope towards the south (left) and cold towards the north (right). Contours plot the proportion of broken waves Q_b; (b) the mean time-averaged rip current speed $\langle uv \rangle$ (black), mean $\langle u \rangle$ (dotted) and maximum offshore flow velocity (dashed); (c) mean water depth h at R8 in the rip channel; and (d) alongshore bathymetric profile (thick line) indicating the MLWS elevation (dashed line) and time-stacks of the mean cross-shore flow velocity $\langle u \rangle$. (For interpretation of the references to colour in this figure caption, the reader is referred to the web version of this paper.)

forces a strong mass flux towards the south from the bar crest along the feeder channel driving the rip current.

Over the low tide maxima, wave breaking across the $Y_m = 1200$ m rip channel falls to $Q_b < 0.5$ as it is shielded by the sub-tidal bar. The positive region of $\partial\eta/\partial y$ to the north of the rip channel is now balanced by a negative (northward acting) region of $\partial\eta/\partial y$ to the south of the channel ($Y_m = 1125$ m), and both are focused and maximised around the ends of the inter-tidal bars. The rip flows offshore as a narrow channelised offshore-directed flow, but the rip speed $\langle uv \rangle$ is reduced from its peak at $t - T = -1.5$ h. The reverse sequence of events occurs during the flood tide.

4.4. Temporal evolution of alongshore non-uniformity

The temporal signature of the alongshore non-uniformities in Q_b, $\partial\eta/\partial y$ and the offshore-directed flow velocity $\langle \overrightarrow{u} \rangle$ can be characterised by their alongshore temporal variance $\sigma^2(t)$ in a similar manner to Feddersen and Guza (2003)

$$\sigma^2_{Q_b}(x,t) = \frac{1}{L_y}\int_0^{L_y} [Q_b(t,y) - \langle Q_b(y) \rangle]^2 \, dy \tag{6}$$

$$\sigma^2_{|\partial\eta/\partial y|}(x,t) = \frac{1}{L_y}\int_0^{L_y} [|\partial\eta/\partial y|(t,y) - \langle |\partial\eta/\partial y|(y) \rangle]^2 \, dy \tag{7}$$

$$\sigma^2_{\overrightarrow{u}}(x,t) = \frac{1}{L_y}\int_0^{L_y} [\overrightarrow{u}(t,y) - \langle \overrightarrow{u}(y) \rangle]^2 \, dy \tag{8}$$

where L_y is the alongshore integration distance ($=1200$ m), dy the alongshore grid spacing ($=5$ m), $\langle \cdot \rangle$ the alongshore-transect temporal average and $|\cdot|$ the modulus.

The nearshore distribution of the alongshore temporal variance $\sigma^2(t)$ highlights the periods when the forcing parameters Q_b and $\partial\eta/\partial y$, and the resultant offshore-directed flow $\langle \overrightarrow{u} \rangle$, display the maximum deviation from their alongshore temporal mean (Fig. 13). As expected, $\sigma^2_{Q_b}$ is maximised across the width of the surf zone, which migrates across the nearshore with the tide. When the rip currents become active, approximately 2 h before the low water minima, peak $\sigma^2_{Q_b}$ is located over the low tide bar/rip morphology and $\sigma^2_{\overrightarrow{u}}$ rapidly increases, peaking $\sim$1–2 h before low water. An hour before low tide, the peak $\sigma^2_{Q_b}$ has migrated seaward of the inter-tidal bar/rip morphology toward the sub-tidal bar and, along with $\sigma^2_{\overrightarrow{u}}$, is reduced over R7 and R8. In contrast, $\sigma^2_{|\partial\eta/\partial y|}$ is negligible over the majority of the domain before becoming highly focused over the inter-tidal bar/rip morphology over low tide. R7 almost dries out at low water and $\sigma^2_{|\partial\eta/\partial y|}$ tends to zero, but in contrast $\sigma^2_{|\partial\eta/\partial y|}$ is maximised at R8, which remains fully submerged. Over the low water minima, $\sigma^2_{\overrightarrow{u}}$ is decreased compared to its peak, but offshore flow is maintained through the rip neck with a variance twice that of the background level (i.e. when the rip currents are not active).

5. Discussion

Detailed field measurements combined with a numerical model investigation demonstrate that rip current strength and behaviour is

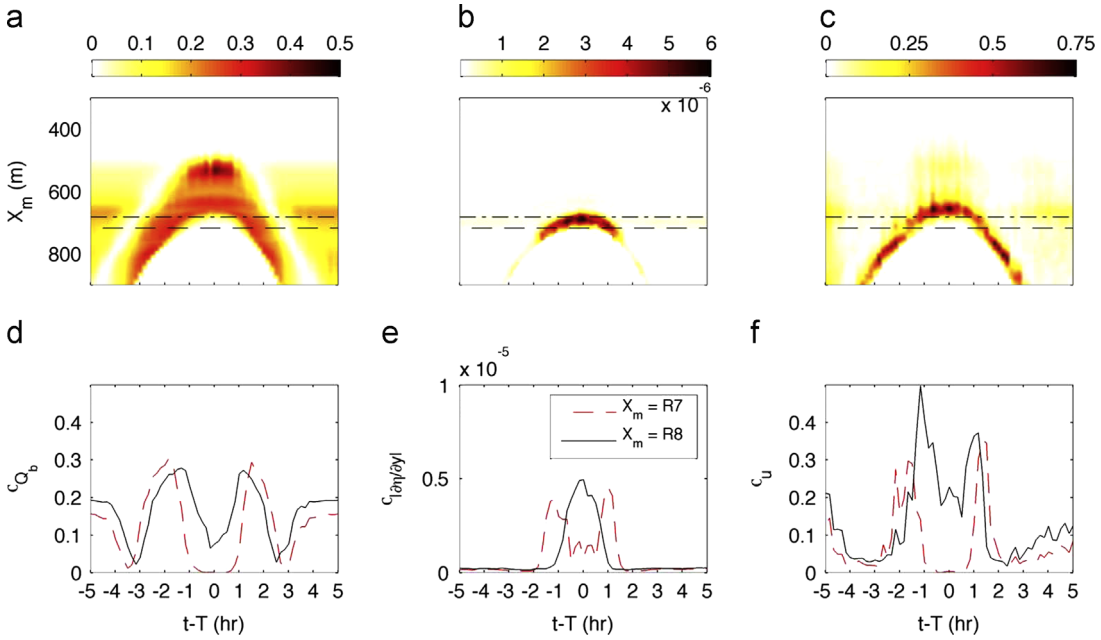

Fig. 13. Temporal alongshore non-uniformity σ^2. (a) Temporal signature of $\sigma^2_{Q_b}$, (b) $\sigma^2_{|\partial\eta/\partial y|}$ and (c) $\sigma^2_{\overrightarrow{\langle u \rangle}}$. The dash and dotted-dash lines indicate the cross-shore position of the rip channel rigs R7 and R8, respectively. (d–e) Evolution of $\sigma^2_{Q_b}$, $\sigma^2_{|\partial\eta/\partial y|}$ and $\sigma^2_{\overrightarrow{\langle u \rangle}}$ at R8 (black) and R7 (red dash). (For interpretation of the references to colour in this figure caption, the reader is referred to the web version of this paper.)

modulated at the semi-diurnal frequency by tide-induced changes in the water level over complex inter- and sub-tidal bar/rip morphology. Three spring low tide cycles when the wave forcing remained approximately constant were analysed, leaving the tide as the main variable factor. In common with other recent observations in similar macro-tidal environments (Bruneau et al., 2009; Austin et al., 2010) rip current flows are maximised around, but not at, low water. At higher tidal elevations, the nearshore is dominated by meandering alongshore-directed currents and bed-return flow.

The mean circulation around the rip system remained fairly consistent with the generally accepted ideas of rip current forcing by radiation stress and pressure gradients (i.e. Bowen and Inman, 1969; Sonu, 1972; MacMahan et al., 2006). The hydrodynamic process signature (Wright and Short, 1984) demonstrates weak onshore flows over the inter-tidal bar crest, which rotate alongshore and strengthen before flowing offshore through the oblique rip channel. Although the rip speeds are high throughout the rip channel, its oblique nature results in a strong alongshore component at the landward end, which becomes more offshore-directed at the rip neck. It also highlights the increased contribution of infragravity-frequency motions in the feeder channel landwards of the bar crest as the incident motions are dissipated. The temporal evolution of the process signature clearly highlights that first the bar crest and then the feeder channel locations are emergent and dry-out over low water. However, although the rip speeds decrease as the forcing from the bar/feeder tends to zero, a significant mean seaward-directed flow persists through the rip channel.

Measured and modelled flow velocities are positively correlated with the alongshore-directed water surface gradients ($\partial\eta/\partial y$) with stronger flows generally observed for larger gradients. Water surface gradients recorded along the feeder channel and at the end of the inter-tidal bar are intensified around low water. Overall, examining the combined flow speed $\langle uv \rangle$ and thus removing the directionality of the resolved $\langle u \rangle$ and $\langle v \rangle$ components, the data scale well with $\partial\eta/\partial y$. However, there is a significant inflection in the curves for $\partial\eta/\partial y \gtrsim 0.5 \times 10^{-3}$, which corresponds with the time of maximum wave dissipation over the bar/rip region and strongest rip speeds $\langle uv \rangle$, observed ~ 1.5 h before low water.

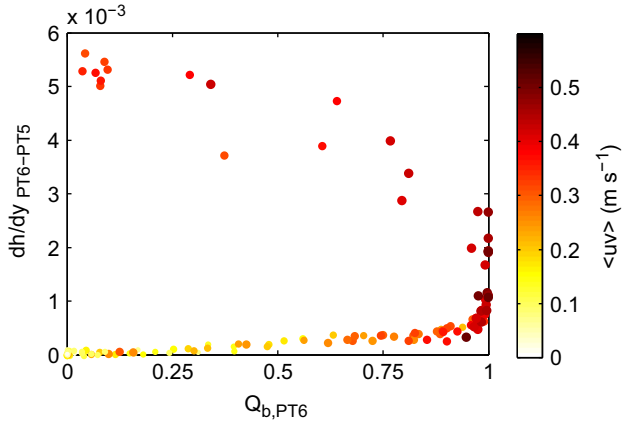

Fig. 14. Scatter plot of modelled rip speed at R8 in $Q_{b,PT6}$ and $|\partial\eta/\partial y|_{PT6-PT5}$ parameter space. Darker shading represents greater flow speed.

The drying of the bar-crest/feeder regions, inflection in the gradient-velocity curves and the slight decrease in observed flow velocities for the peak gradients observed at low water suggest that there is more than one factor forcing the rip currents and that the balance between them changes approaching low tide. Model outputs of $\partial\eta/\partial y$ and Q_b over the entire domain at two key time steps approaching low water (Fig. 11) demonstrate an decrease in Q_b over the inter-tidal bar and feeder regions in the period $t-T=-2$ to -1. At the same time there is a coincident increase in $\partial\eta/\partial y$, strongly focused around the ends of the bar (along the sides of the rip channel) and the currents within the rip channel rotate offshore flowing normal to the plane between the maxima and the minima of $\partial\eta/\partial y$. This is clearly demonstrated in Fig. 14, which plots $\langle uv \rangle$ in the rip channel in Q_b–$\partial\eta/\partial y$ parameter space, showing that $\langle uv \rangle$ and $\partial\eta/\partial y$ are low until Q_b exceeds ~ 0.75. $\partial\eta/\partial y$ increases rapidly once $Q_b \gtrsim 0.9$ and $\langle uv \rangle$ is approximately maintained, but then as $\partial\eta/\partial y$ is maximised there is clear hysteresis and Q_b rapidly tends to zero and $\langle uv \rangle$ is reduced.

Examining $\partial\eta/\partial y$ over the alongshore transect through the rip channel (Fig. 12) clearly shows the development of the alongshore

gradients and the link with Q_b. When wave breaking over the bar/rip is minimal $\partial\eta/\partial y$ is small, but as Q_b increases so does $\partial\eta/\partial y$. Initially a strong positive (southward acting) gradient forms, which is not balanced by an equivalent negative gradient and a broad rip current flows to the south. This is probably the result of the morphological dominance of the northerly feeder channel and its pressure-driven current. Moving towards low water, the bar becomes increasingly emergent and the forcing from the feeder decreases as it dries-out, but the local alongshore gradients around the bar ends intensify. The opposing positive and negative gradients now almost balance and the rip current becomes focussed into the centre of the rip channel and offshore flow is maintained, albeit at a reduced speed. The temporal alongshore non-uniformities show similar behaviour.

Previous field data from micro- (Brander, 1999) and meso-tidal (Brander and Short, 2000; Bruneau et al., 2011) environments also appear to indicate the occurrence of peak rip flow immediately either side of low water, rather than at low water; these observations were not stressed at the time. Brander (1999) states the underlying hypothesis that rip flow is maximised when the morphological expression of the rip channel is also maximised, as it is at low water. However, these previous observations, together with those of Austin et al. (2010) and the present work, suggest that whilst maximising the expression of the channel morphology does increase rip flow speed, at the low water minimum the forcing is reduced to such an extent that the flow decreases.

At low water, the rip channel becomes morphologically isolated from the feeder channels. The minimal wave dissipation across the rip, combined with the continued wave breaking along the edge of the rip channel, indicates an increase in local set-up ($\partial\eta/\partial y$) at the bar ends, forcing water to drain into the rip channel; this supports the previous field observations (Brander, 1999; Austin et al., 2010; Bruneau et al., 2011). The weakening of the flow directly around low water may be linked to two factors: (1) the limited spatial extent of $\partial\eta/\partial y$ around the ends of the bar; and (2) to a change in the balance of the alongshore pressure gradient force generated at the ends of the bars and the opposing radiation stress gradient in the rip channel forced by relatively larger waves (Haller et al., 2002), that have reformed while propagating up the rip channel after initially breaking over the sub-tidal bar.

An interesting alternative explanation for the spatially confined rip flow at low water is the generation of vorticity by short-crested breaking waves along the terminal ends of the bars (Clark et al., 2012). Opposing left- and right-breaking waves along the sides of the rip channel form counter-rotating vortices that maintain the rip flow around low water; the spatially constrained dissipation limits the vorticity generation and hence the flow speed.

6. Conclusions

Water-level controls on macro-tidal rip current dynamics were investigated through field measurements and numerical modelling. Field data, spanning a range of wave and tide conditions, demonstrate that rip current strength and behaviour is modulated at the semi-diurnal frequency by tide-induced changes in the water-level over bar/rip morphology. Peak flow speeds $\langle uv\rangle$ were observed in the rip neck 1.5 h before and after low water, corresponding to the time when wave dissipation was maximised over the bar/feeder region. When the inter-tidal bar and feeder were dry around low water, rip flow was maintained, but $\langle uv\rangle$ was reduced.

The development of alongshore-directed water surface gradients $\partial\eta/\partial y$ along the feeder channel and at the bar ends was observed from $\sim$4 h before low water; $\partial\eta/\partial y$ was maximised approximately 1.5 h before low water. A positive correlation between $\partial\eta/\partial y$ and $\langle uv\rangle$ was observed, which appears to correspond to the time of maximum wave-breaking over the bar/rip region; above this value, $\langle uv\rangle$ remains constant or decreases.

The numerical model was able to reproduce $\partial\eta/\partial y$ with a good level of skill and demonstrated a dependence of $\partial\eta/\partial y$ and $\langle uv\rangle$ on the proportion of breaking waves Q_b. Spatially, across the bar/rip region, once $Q_b \geq 0.75$, $\partial\eta/\partial y$, $\langle uv\rangle$ increased; however, peak $\partial\eta/\partial y$ was observed when Q_b decreased as wave breaking moved offshore to the sub-tidal bar approximately 1-hour before low water.

The reduction in Q_b over the bar and feeder regions decreased the pressure-driven feeder current, but offshore flow through the rip channel was maintained by a localised intensification of $\partial\eta/\partial y$ around the ends of the inter-tidal bar. Around low water, the peak temporal alongshore non-uniformity of Q_b is located over the sub-tidal bar, whereas $\partial\eta/\partial y$ is maximised over the rip channel maintaining offshore flow through the rip channel. Future field and numerical studies of $\partial\eta/\partial y$ over a more spatially dense array will be crucial to further improve our understanding of rip circulation in very shallow waters, the exchange between inter- and sub-tidal bar rips and to investigate the potential role of short-crested breaking wave vorticity.

Acknowledgements

We would like to thank our excellent field and technical team: Peter Ganderton, Anthony Thorpe, Claire Earlie, Ellie Woodward, Tim Poate, Robert McCall, Megan Sheriden, Ivan Burton, Richard Kenyon, Pedro Almeida, Hanna Richardson, Jak McCarroll, Kit Stokes, Barbara Proenca, Joana van Nieuwkoop, Ruth Stafford, Matt Hilton, Bruno Castelle, Nicolas Bruneau, Dano Roelvink, Ap van Dongeren, Leo Sembiring, Jack Puleo, Mark Davidson, Iain Fairley, Fran Sieck, Emily Beaumont and Jon Miles. We would also like to thank the RNLI, and in particular Dickon Berriman, for their assistance at Perranporth. Phil Maynard from the Perranporth YHA is also thanked for his ongoing assistance. This research was funded by the NERC-RNLI partnership grant NE/H004262/1, Dynamics of Rip Currents and Implications for Beach Safety. We also acknowledge the constructive comments made by several reviewers.

References

Austin, M.J., Scott, T.M., Brown, J.W., Brown, J.A., MacMahan, J.H., Masselink, G., Russell, P.E., 2010. Temporal observations of rip current circulation on a macro-tidal beach. Cont. Shelf Res. 30 (9), 1149–1165.

Austin, M.J., Scott, T.M., Russell, P.E., Masselink, G., 2013. Rip current prediction: development, validation and evaluation of an operational tool. J. Coast. Res. 29 (2), 283–300.

Bowen, A.J., 1969. Rip currents, 1. Theoretical investigations. J. Geophys. Res. 74, 5467–5478.

Bowen, A.J., Inman, D., 1969. Rip currents, 2. Laboratory and field observations. J. Geophys. Res. 74 (23), 5479–5490.

Brander, R.W., 1999. Field observations on the morphodynamic evolution of a low-energy rip current system. Mar. Geol. 157 (3–4), 199–217.

Brander, R.W., Short, A.D., 2000. Morphodynamics of a large-scale rip current system at Muriwai Beach, New Zealand. Mar. Geol. 165 (1–4), 27–39.

Bruneau, N., Bonneton, P., Castelle, B., Pedreros, R., 2011. Modeling rip current circulations and vorticity in a high-energy mesotidal–macrotidal environment. J. Geophys. Res. 116 (July (C7)), 1–17.

Bruneau, N., Castelle, B., Bonneton, P., Pedreros, R., Almar, R., Bonneton, N., Bretel, P., Parisot, J.-P., Sénéchal, N., 2009. Field observations of an evolving rip current on a meso-macrotidal well-developed inner bar and rip morphology. Cont. Shelf Res. 29, 1650–1662.

Castelle, B., Bonneton, P., Senechal, N., Dupuis, H., Butel, R., Michel, D., 2006. Dynamics of wave-induced currents over an alongshore non-uniform multiple-barred sandy beach on the Aquitanian Coast, France. Cont. Shelf Res. 26 (January (1)), 113–131.

Clark, D.B., Elgar, S., Raubenheimer, B., 2012. Vorticity generation by short-crested wave breaking. Geophys. Res. Lett. 39 (24), http://dx.doi.org/10.1029/2012GL054034.

Daly, C., Roelvink, J.A., van Dongeren, A., van Thiel de Vires, J., McCall, R.T., 2012. Validation of an advective-deterministic approach to short wave breaking in a surf beat model. Coast. Eng. 60, 69–83.

Deigaard, R., 1993. A note on the three dimensional shear stress distribution in a surf zone. J. Coast. Res. 20, 157–171.
Feddersen, F., Guza, R.T., 2003. Observations of nearshore circulation: alongshore uniformity. J. Geophys. Res. 108 (C1), http://dx.doi.org/10.1029/2001JC001293.
Haas, K., Svendesen, I.A., Haller, M.C., Zhao, Q., 2003. Quasi-three-dimensional modeling of rip current systems. J. Geophys. Res. 108 (C7), 3217, http://dx.doi.org/10.1029/2002JC001355.
Haller, M., Dalrymple, R., 2001. Rip current instabilities. J. Fluid Mech. 433, 161–192.
Haller, M., Dalrymple, R., Svendesen, I., 2002. Experimental study of nearshore dynamics on a barred beach with rip channels. J. Geophys. Res. 107 (14), 1–21.
MacMahan, J., Thornton, E., Reniers, A.J.H.M., 2006. Rip current review. Coast. Eng. 53 (2–3), 191–208.
MacMahan, J.H., Brown, J., Thornton, E.B., 2009. Low-cost hand-held global positioning system for measuring surf zone currents. J. Coast. Res. 25 (3), 744–754.
MacMahan, J.H., Reniers, A., Thornton, E.B., Stanton, T.P., 2004. Infragravity rip current pulsations. J. Geophys. Res. 109 (C01033), http://dx.doi.org/10.1029/2003JC002068.
MacMahan, J.H., Thornton, E.B., Reniers, A.J.H.M., Stanton, T.P., Symonds, G., 2008. Rip currents induced by small bathymetric variations. Mar. Geol. 255 (3–4), 156–164.
Masselink, G., Short, A.D., 1993. The effect of tide range on beach morphodynamics and morphology. J. Coast. Res. 9, 785–800.
McKenzie, P., 1958. Rip-current systems. J. Geol. 66 (2), 103–113.
Nielsen, P., Brander, R.W., Hughes, M.G., 2001. Rip currents: observations of hydraulic gradients, friction factors and wave pump efficiency. In: Hanson, H., Larson, M. (Eds.), Coastal Dynamics '01. ASCE, Lund, Sweden, pp. 483–492.
Plant, N.G., Holland, K., Puleo, J.A., 2002. Analysis of the scale of errors in nearshore bathymetric data. Mar. Geol. 191 (November (1–2)), 71–86.
Reniers, A.J.H.M., MacMahan, J.H., Thornton, E.B., Stanton, T.P., 2006. Modelling infragravity motions on a rip-channel beach. Coast. Eng. 53 (2–3), 209–222.
Roelvink, D., Reniers, A., van Dongeren, A., van Thiel de Vries, J., McCall, R., Lescinski, J., 2009. Modelling storm impacts on beaches, dunes and barrier islands. Coast. Eng. 56 (November (11–12)), 1133–1152.
Schmit, W.B., Woodward, K., Millikan, R., Guza, R.T., Raubenheimer, B., Elgar, S., 2003. A GPS-tracked surf zone drifter. J. Atmos. Ocean Technol. 20, 1069–1075.
Scott, T.M., Masselink, G., Russell, P.E., 2011. Morphodynamic characteristics and classification of beaches in England and Wales. Mar. Geol. 286, 1–20.
Sonu, C.J., 1972. Field observation on nearshore circulation and meandering currents. J. Geophys. Res. 77, 3232–3247.
Spydell, M., Feddersen, F., Guza, R.T., Schmit, W.E., 2007. Observing surf-zone dispersion with drifters. J. Phys. Oceanogr. 37 (12), 2920–2939.
Wright, L.D., Short, A.D., 1984. Morphodynamic variability of surf zones and beaches: a synthesis. Mar. Geol. 56, 93–118.
Yu, J., Slinn, D.N., 2003. Effects of wave–current interaction on rip currents. J. Geophys. Res. 108, 3088, http://dx.doi.org/10.1029/2001JC001105.